

Construction of exfoliated g-C₃N₄ nanosheets–BiOCl hybrids with enhanced photocatalytic performance†

Cite this: *RSC Adv.*, 2014, 4, 28519

Fei Chang,^{*a} Yunchao Xie,^a Jian Zhang,^a Juan Chen,^a Chenlu Li,^a Jie Wang,^a Jieru Luo,^a Baoqing Deng^a and Xuefeng Hu^{*b}

Exfoliated g-C₃N₄ nanosheets (CNs) were composited with bismuth oxychloride (BiOCl) to fabricate a series of hybrids *via* a facile chemical deposition–precipitation method in this investigation. The as-synthesized BiOCl–CNs hybrids were then fully characterized by a collection of analytical techniques. It was obviously observed that CNs were in intimate contact with hierarchical BiOCl flowerlike units to form heterojunction structures, which facilitates transfer and efficient separation of photoinduced electron–hole pairs, thus greatly increasing catalytic activity upon visible light irradiation. Together with other merits such as enlarged specific surface area, favorable optical properties, and suitable energy-band structures, these robust BiOCl–CNs hybrids showed significantly enhanced photocatalytic performance towards Rhodamine B (RhB) dye removal. Under identical conditions, the apparent photocatalytic reaction rate of the best hybrid BiOCl–CNs–3% was about 2.1 and 26.6 times as high as those of BiOCl and CNs alone, respectively. A possible photocatalytic mechanism was also proposed by means of active species trapping measurements, revealing that superoxide radicals ([•]O₂[−]) played a crucial role during the catalytic process.

Received 28th March 2014
Accepted 5th June 2014

DOI: 10.1039/c4ra02735c

www.rsc.org/advances

1. Introduction

The construction of heterojunction structures between two different components is deemed as an efficient strategy for developing diverse hybrid materials with multiple functionalities, especially in photocatalysis.^{1,2} Different semiconductors with suitable conduction and valence band edges are integrated within the same structure, favoring the transfer and separation, and thus depressed recombination of photoinduced charge carriers between the different components. Accordingly, photocatalytic performance of hybrids can be greatly improved in comparison to those of the individual catalysts.^{3,4} Though enormous efforts have been exerted in this field, it is still a challenge to fabricate efficient heterojunction photocatalysts featuring visible light response, excellent catalytic activity, and satisfactory stability as well as low cost.

BiOCl, a well-known bismuth-based semiconductor, crystallizes in a tetragonal matlockite structure, a lamellar structure

characterized with [Bi₂O₂] slabs interleaved by two slabs of chlorine atoms,⁵ which is beneficial to inhibiting recombination of charge carriers.⁶ With other favorable structural merits, BiOCl exhibited even much better catalytic performance than P25 (Degussa TiO₂), a commercial catalyst usually utilized as a standard during photocatalytic measurements.⁵ Therefore, BiOCl with unique and excellent electrical and optical properties has been drawing increasing research interests.^{5,7–9} However, BiOCl is of wide band gap (3.2–3.6 eV) and hereby can only be excited by ultraviolet irradiation, instead of visible light that is abundant in nature, which drastically limits its effective applications in visible light region.⁷ To solve this problem, diverse semiconductors with narrow band gaps that can absorb visible light, such as Bi₂WO₆,⁸ BiOI,^{2,9} BiOBr,¹⁰ and NaBiO₃,¹¹ have been selected to hybridize with BiOCl to prepare heterojunction hybrids, aiming to drive photocatalytic reactions under visible light irradiation.

Most recently, Wang *et al.* reported that g-C₃N₄ could be utilized as an efficient visible-light-driven photocatalyst for hydrogen evolution by water splitting.¹² Unlike other metal-containing photocatalysts, g-C₃N₄ is a sustainable and environmentally friendly organic semiconductor consisting of carbon, nitrogen, and hydrogen atoms only.^{1,13} It is expressly thermal and photochemical stable owing to the high polymeric degree and π-conjugated structure and can thus undergo photocatalysis under visible light without modification.¹⁴ However, bare g-C₃N₄ materials suffer from high recombination rate of

^aSchool of Environment and Architecture, University of Shanghai for Science and Technology, Shanghai, 200093, P.R. China. E-mail: feichang@usst.edu.cn; Tel: +86-21-55271722

^bKey Laboratory of Coastal Zone Environmental Processes and Ecological Remediation, Yantai Institute of Coastal Zone Research, Chinese Academy of Sciences, Yantai, Shandong, 264003, P.R. China. E-mail: xfhu@yic.ac.cn; Tel: +86-535-2109157

† Electronic supplementary information (ESI) available. See DOI: 10.1039/c4ra02735c

electron-hole pairs and accordingly display relatively low photocatalytic efficiency, hindering its further applications. Several strategies have been adopted to raise the catalytic activity of $g\text{-C}_3\text{N}_4$, including introduction of mesoporous structure,^{15,16} doping with metal or nonmetal elements,^{20,21} coupling with other semiconductors,^{1,22,23} as well as exfoliation of bulk phase to nanosheets.^{17–19} During exfoliation, multilayered $g\text{-C}_3\text{N}_4$ tends to grow thin in thickness and thus may create new exposed surface, leading to the inhibition of photoinduced charge carriers recombination, large specific surface area, and blue shift of light absorption edge, which significantly influence photocatalytic performances. Niu *et al.* demonstrated that $g\text{-C}_3\text{N}_4$ nanosheets by a thermal etching method showed remarkably enhanced photocatalytic H_2 evolution efficiency comparing to bulk $g\text{-C}_3\text{N}_4$.¹⁷ Xu *et al.* reported that single-layered $g\text{-C}_3\text{N}_4$ nanosheets *via* a simple chemical exfoliation route exhibited much higher photocatalytic H_2 production and pollutant decomposition activities than bulk $g\text{-C}_3\text{N}_4$.¹⁸ Yang *et al.* indicated that free-standing $g\text{-C}_3\text{N}_4$ nanosheets *via* a liquid phase exfoliation technique displayed higher photocatalytic performance of H_2 evolution than bulk $g\text{-C}_3\text{N}_4$.¹⁹ Hence, it is reasonable to realize that $g\text{-C}_3\text{N}_4$ nanosheets are indeed superior to bulk $g\text{-C}_3\text{N}_4$ under identical conditions in terms of photocatalytic performance.

It is found that energy levels of bulk $g\text{-C}_3\text{N}_4$ and BiOCl are well-matched and can overlap in band structure, suiting to construct heterojunction catalysts with visible light response.^{5,12,20,21} Therefore, a few references have been reported to synthesize and evaluate photocatalytic performance of bulk $g\text{-C}_3\text{N}_4\text{-BiOCl}$ hybrids.^{22,23} However, to the best of our knowledge, there were no reports demonstrating synthesis and application of BiOCl hybridized with exfoliated $g\text{-C}_3\text{N}_4$ nanosheets for pollutants removal under visible light irradiation, even exfoliated $g\text{-C}_3\text{N}_4$ nanosheets showed outstanding catalytic performance in comparison to bulk $g\text{-C}_3\text{N}_4$. Therefore, in this study, for the first time, novel and robust BiOCl-CNs hybrids were synthesized through a facile chemical deposition-precipitation method and then exposed to photocatalytic degradation of dye RhB. Excellent photocatalytic performance of BiOCl-CNs series was achieved and attributed to the enlarged specific surface area, favorable optical property, and suitable energy-band structures as well. In addition, a possible mechanism for enhancing photocatalytic activity of BiOCl-CNs hybrids was also proposed through active species trapping measurements.

2. Experimental

2.1 Chemicals

All chemicals in this study were purchased from Sinopharm Chemical Reagent Co., Ltd. and used directly for experiments without any further purification. Deionized water was used throughout the experiments.

2.2 Synthesis of BiOCl-CNs hybrids

Synthetic procedure of CNs from bulk $g\text{-C}_3\text{N}_4$ (CNb) was provided in detail in ESI† section.

A typical protocol for preparing BiOCl-CNs hybrids was described as follows: a measured amount of CNs and $\text{Bi}(\text{NO}_3)_3 \cdot 5\text{H}_2\text{O}$ (1.86 g) were added into a mixture of HCl aqueous solution (2 M, 25 mL), deionized water (20 mL), and *n*-propanol (10 mL) and then the resultant mixture was ultrasonicated for 0.5 h to obtain a uniform suspension, which was gradually transformed into a white suspension in advance of adding NaOH aqueous solution (4 M, 20 mL) by dropwise. After stirred for another 0.5 h and aged for 6 h, the resulted precipitate was collected by centrifugation, washed thoroughly with water and ethanol, and then dried at 100 °C overnight. Finally, the produced BiOCl-CNs hybrids were ground for further characterization and use. According to this method, a series of BiOCl-CNs hybrids with mass ratios from 1% to 5% were prepared and denoted as BiOCl-CNs-*x*%, where *x* referred to the mass ratio of CNs to BiOCl. Pure BiOCl was synthesized under an identical condition in absence of CNs. Sample BiOCl-CNb-3% was prepared using a same procedure stated above except that CNs was replaced by CNb. As a reference, a mechanically mixed BiOCl-CNs-3% was also prepared by finely grinding a mixture of CNs and BiOCl with a desired mass ratio, denoted as BiOCl-CNs-3% (blend).

2.3 Characterization

X-ray diffraction (XRD) patterns were recorded on a Bruker D8 Advance X-ray diffractometer using a $\text{Cu K}\alpha$ radiation source ($\lambda = 1.05406 \text{ \AA}$). The surface morphology was observed by scanning electron microscope (SEM, Hitachi S4800 and Hitachi S4700). TEM, HRTEM patterns, and SAED images were recorded on a FEI Tecnai G² F20 transmission electron microscope operated at 200 kV. HRTEM was analyzed using the Digital Micrograph software (Gatan Inc.). The Fourier transform infrared spectra (FT-IR) were collected on a Thermo Nicolet Avatar 370 using the standard KBr disk method. UV-vis diffuse reflection spectroscopy (UV-vis DRS) was obtained on a Shimadzu UV2600 spectrophotometer using BaSO_4 as a reference. Nitrogen adsorption-desorption isotherms at 77 K was carried on a Micromeritics ASAP 2020 nitrogen adsorption apparatus. X-ray photoelectron spectroscopy (XPS) measurements were performed on a RBD upgraded PHI 5000C ESCA System (Perkin Elmer) with an $\text{Mg K}\alpha$ (1253.6 eV) radiation. Binding energies were calibrated by using the containment carbon (C 1s = 284.6 eV). The solid photoluminescence spectra (PL) were detected on a Shimadzu RF-5301PC spectrometer.

2.4 Photocatalytic activity measurement

Photocatalytic activity of as-synthesized BiOCl-CNs hybrids were evaluated towards degradation of dye RhB and 2,4-dichlorophenoxyacetic acid (2,4-D) under visible light illumination in a LIMX-VII apparatus by Bylabo Precision Instrument Co. Ltd. (Xi'an, China). Visible light was supplied by a 400 W halogen lamp, equipping with a sodium nitrite solution (2 M) to eliminate UV light ($\lambda < 400 \text{ nm}$) and thermal effect.^{24,25} Catalyst (20 mg) was dispersed in an aqueous solution of RhB (50 mg L^{-1} , 40 mL) or 2,4-D (15 mg L^{-1} , 40 mL) and the suspension was magnetically stirred for 1 h in dark to ensure an adsorption-

desorption equilibrium before exposure to visible light. The photocatalytic efficiency was attained through measurement of the absorbance band of RhB at 554 nm after a fixed interval time. The absorbance measurement of reaction solutions was conducted using a Shimadzu UV2600 spectrophotometer after separating catalyst particles from 3.5 mL aliquots by centrifugation. 2,4-D was analyzed by a Waters e2569 HPLC equipped with a Waters reverse-phase C18 column (4.6 mm × 150 mm, 3.5 μm, XBridge, Ireland) and a Waters 2489 UV-vis detector. The mobile phase (flow rate 0.3 mL min⁻¹) was a mixture of methanol and ultrapure water (55 : 45, v/v, pH = 3), the water being acidified with concentrated acetic acid. The maximum absorption wavelength was detected at 290 nm.

The effects of several active radical species on the photocatalytic system were investigated to understand the photocatalytic mechanism. A typical procedure was depicted as below: during the photocatalytic process in the presence of BiOCl-CNs-3% hybrid as a catalyst, 1.0 mM isopropanol (IPA), 1,4-benzoquinone (BQ), or disodium ethylenediaminetetraacetate dihydrate (EDTA-2Na) was added aiming to capture hydroxyl radicals ([•]OH), superoxide radicals ([•]O₂⁻), or holes (h⁺), respectively.^{26–28} N₂ bubbling experiment was also accomplished through expelling dissolved oxygen with bubbling N₂ gas.

The measurement of [•]OH amount was also conducted according to the literature. A Shimadzu RF-5301 PC fluorescence spectrophotometer was used to measure the fluorescence signal of generated 2-hydroxy terephthalic acid (TAOH). The excitation light employed during recording fluorescence spectra was 320 nm.²⁷

The stability, reusability, and durability of BiOCl-CNs-3% hybrid were estimated according to a following procedure: after each run, the catalyst was collected from aqueous solution by centrifugation, washed with deionized water and ethanol under ultrasonication for several times, and dried overnight at 100 °C. Afterwards, each recycling test was performed and checked using a same procedure that we have described above.

3. Results and discussion

The CNs was carefully exfoliated from parent bulk g-C₃N₄ using a thermal oxidation etching method.¹⁷ The CNs in light yellow and bulk g-C₃N₄ in yellow with an identical mass were shown in Fig. S1.† The XRD patterns of CNs in Fig. S2A† show two characteristic peaks in good agreement with those of bulk g-C₃N₄. The weakened diffraction peak (002) at 27.7° strongly reveals the exfoliation of bulk form to nanosheets in morphology.^{29,30} The FT-IR spectrum of CNs is quite similar to that of bulk g-C₃N₄, as seen in Fig. S2B.† Relatively flat and smooth surface of CNs SEM and TEM images with crimped edges are found in Fig. S2C and S2D† in comparison to those of bulk g-C₃N₄ in Fig. S2E and S2F.† The AFM image of sample CNs in Fig. S3† shows well separated nanosheets with a thickness of around 1.9 nm, suggesting the formation of *ca.* six-layered structure. Besides, formation of CNs is also confirmed by the blue shift of main adsorption edge in Fig. S4,† which can be presumably ascribed to the decreased conjugation length and quantum

confinement effect due to decreased thickness.¹⁸ All features above confirm the preservation of basic aromatic tri-s-triazine ring structure and formation of nanosheets after the exfoliation treatment.

3.1 XRD patterns

X-ray power diffraction patterns were measured to investigate phase structures of pure BiOCl and BiOCl-CNs hybrids in Fig. 1. It is obvious that all as-synthesized samples are well crystallized. As evident from Fig. 1, pure BiOCl displays a series of diffraction peaks, indexing to a *P4/nmm* tetragonal phase with lattice constants of *a* = *b* = 3.891 Å, and *c* = 7.369 Å, according to the standard card JCPDS 06-0249.³¹ After hybridization with CNs, BiOCl-CNs hybrids show no apparent changes in XRD patterns, indicating the maintenance of basic BiOCl phase structure. However, characteristic diffraction peaks of CNs cannot be detectable in these BiOCl-CNs hybrids, probably due to the low content and relatively low diffraction intensity of CNs. In addition, there are no any impurity peaks in these hybrids, revealing the high-purity of synthesized BiOCl-CNs catalysts without formation of byproducts.

3.2 Morphology and microstructure

Fig. 2 shows representative SEM images of bare BiOCl and BiOCl-CNs-3% hybrid. It is observable that hierarchical flowerlike BiOCl units (Fig. 2A and B) are composed of numerous of nanoplates with a diameter of ~0.15 μm and a thickness of ~10 nm. After hybridization *via* a chemical deposition-precipitation method, the morphology of hierarchical flowerlike BiOCl units is still remained in BiOCl-CNs-3% hybrid (Fig. 2C and D), suggesting that the introduction of CNs could not apparently affect the self-assembly process of BiOCl from nanoplates to flowerlike units. Aggregated CNs are irregular in shape and small in size comparing to BiOCl nanoplates and closely attached to the surface of BiOCl nanoplates, marked by white arrows in Fig. 2D. The detail views on the morphology of sample BiOCl and all hybrids are shown in SEM images (Fig. S5†) and

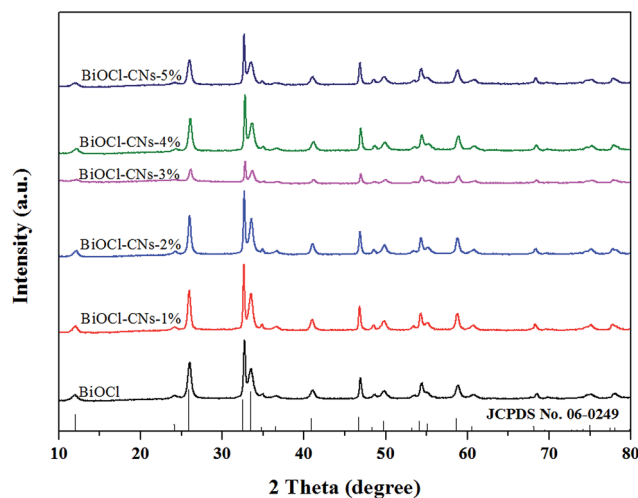


Fig. 1 XRD patterns of BiOCl-CNs hybrids, bare BiOCl, and CNs.

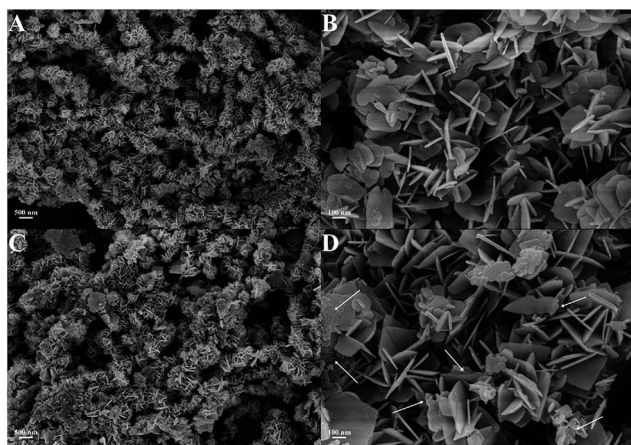


Fig. 2 SEM images of (A) bare BiOCl and (C) BiOCl-CNs-3% hybrid; enlarged SEM images of (B) bare BiOCl and (D) BiOCl-CNs-3% hybrid.

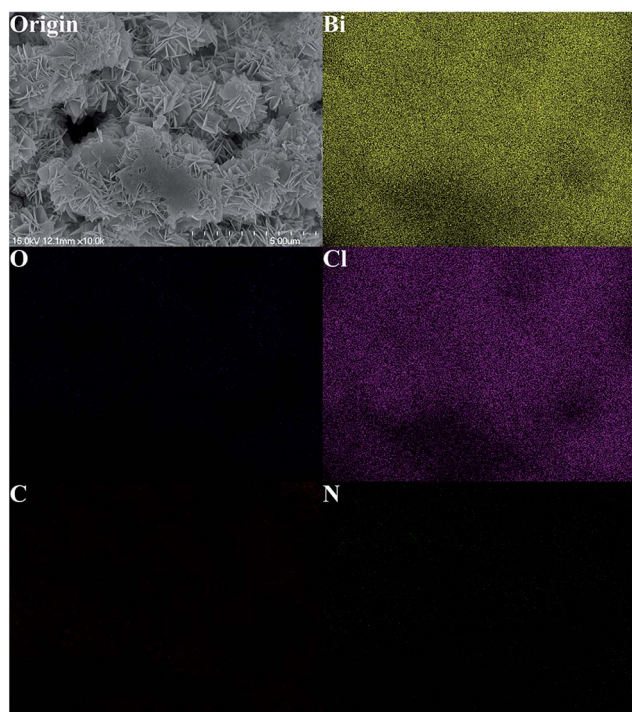


Fig. 3 SEM image and elemental mapping images of BiOCl-CNs-3% hybrid.

TEM images (Fig. S6†). Obviously, all samples display hierarchical flowerlike clusters that are a little variable in size. In addition, the package of nanoplates is slightly loose in hybrids BiOCl-CNs-4% and BiOCl-CNs-5%. Moreover, distribution of BiOCl and CNs in BiOCl-CNs-3% hybrid was analyzed through SEM images and X-ray mapping of elements Bi, O, C, Cl, and N, as seen in Fig. 3. All elements are detectable and distributed evenly, confirming that phase CNs is in good dispersion in hybrid and hereby heterojunction structures are easily formed.

Fig. 4A depicts the microstructures of BiOCl-CNs-3% hybrid in TEM image, consisting of numerous uniform nanoplates with a diameter around 0.15 μm that is well consistent with SEM results. Polycrystalline rings resulting from crystalline particles are obtained by the SAED technique (inset of Fig. 4A). Fig. 4B shows the high-resolution TEM image of the BiOCl-CNs-3% hybrid. Three different kinds of lattice fringes are clearly observed through measuring the lattice parameters *via* Digital Micrograph software and comparing with the data in JCPDS files. The interplanar spacing of around 0.326 nm corresponds to the distance between adjacent (002) crystal planes of $g\text{-C}_3\text{N}_4$ (JCPDS 87-1526).¹² The lattice spaces of 0.220 and 0.344 nm are in good agreement with *d*-values of (112) and (101) crystallographic planes of BiOCl (JCPDS 06-0249), respectively.⁵ From the HRTEM image of BiOCl-CNs-3% hybrid, both phases of CNs and BiOCl coexist and are in close contact to form a smooth and intimate interface along boundaries, confirming that heterojunction structures between CNs and BiOCl indeed formed. The intimate interfaces role as charge carriers channels, by which charge carriers are prone to migrate and separate between semiconductors CNs and BiOCl, efficiently depressing the recombination of photogenerated electron-hole pairs and thus remarkably improving photocatalytic performance.^{1,32} Moreover, this result is powerful evidence that hybridized BiOCl-CNs composites are of heterojunctions in microstructures rather than a physical mixture of two separate phases.

3.3 FT-IR spectra

FT-IR spectra in Fig. 5 display a comparison of BiOCl-CNs hybrids to bare BiOCl and CNs in chemical structures. In CNs-containing samples, a broad band at around 3450 cm^{-1} corresponds to stretching and bending vibrations of O-H, associating with absorbed H_2O molecules.¹³ The absorption band centered at 3200 cm^{-1} of CNs is attributed to the stretching vibration of N-H.³³ A strong absorption band in the range of

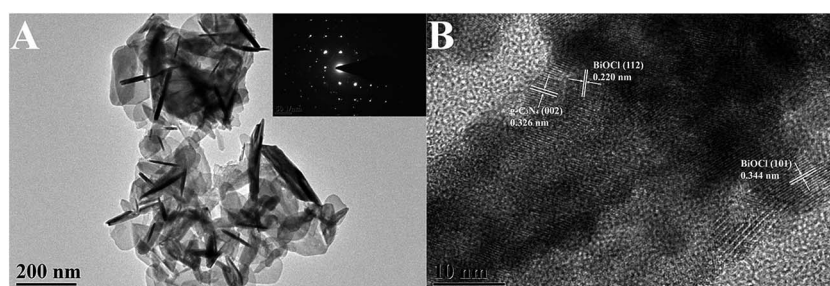


Fig. 4 TEM image (A) and HRTEM image (B) of BiOCl-CNs-3% hybrid (inset of A is SAED analysis).

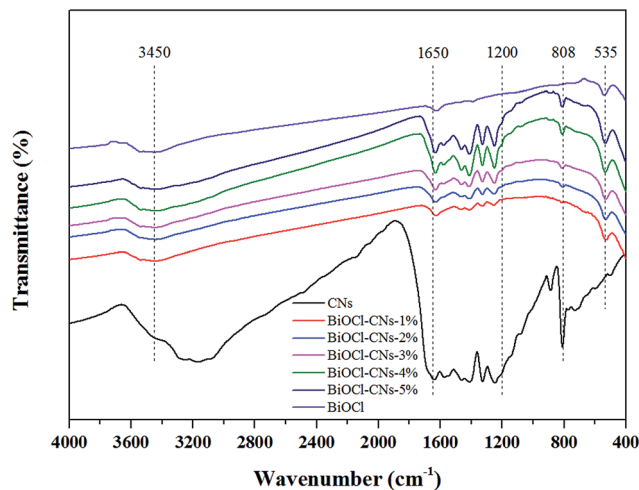


Fig. 5 FT-IR spectra of BiOCl-CNs hybrids, bare BiOCl, and CNs.

1200–1650 cm^{-1} is assigned to typical skeletal stretching vibrations of the *s*-triazine or tri-*s*-triazine,^{33–35} which are fully present in these BiOCl-CNs hybrids, indicating the maintenance of *g*- C_3N_4 basic structure after hybridization. The sharp peak centered at 808 cm^{-1} is relevant to the characteristic breathing mode of triazine units.³⁶ The absorption peak at 535 cm^{-1} is indexed to the Bi-O stretching vibration in a

tetragonal phase BiOCl crystal.³⁷ Further observation finds that the stepwise increase in intensity and slight shift of the band at 1200–1600 cm^{-1} and 808 cm^{-1} from hybrid BiOCl-CNs-1% to BiOCl-CNs-5%, possibly owing to an intense interaction between CNs and BiOCl phases with the increase of CNs content. This intense interaction is essential to transfer and separate charge carriers and accordingly enhance the photocatalytic activity of hybrids.

3.4 XPS spectra

XPS measurements were performed to explicate the surface chemical composition and chemical states of bare BiOCl, CNs, and BiOCl-CNs-3% hybrid, as seen in Fig. 6. Peak positions in all XPS spectra were calibrated with C 1s at 284.6 eV. From the survey XPS spectrum in Fig. 6A, the BiOCl-CNs-3% hybrid consists of Bi, O, C, Cl and N elements, which is well consistent with the chemical composition. High resolution spectra of Bi 4f, Cl 2p, O 1s, C 1s, and N 1s are shown in Fig. 6B–D. After fitting, two strong peaks of bare BiOCl at 159.0 eV and 164.3 eV in Fig. 6B are respectively attributed to Bi 4f_{7/2} and Bi 4f_{5/2} that are characteristics of Bi³⁺ species in BiOCl network.⁸ Peaks with binding energies at 198.1 eV and 199.6 eV correspond to Cl 2p_{3/2} and Cl 2p_{1/2}, and these are characteristics of Cl⁻ anions in bare BiOCl.³⁸ The O 1s core level spectrum in Fig. 6C can be fitted well with two peaks at 530.8 eV and 531.9 eV, relating to O²⁻

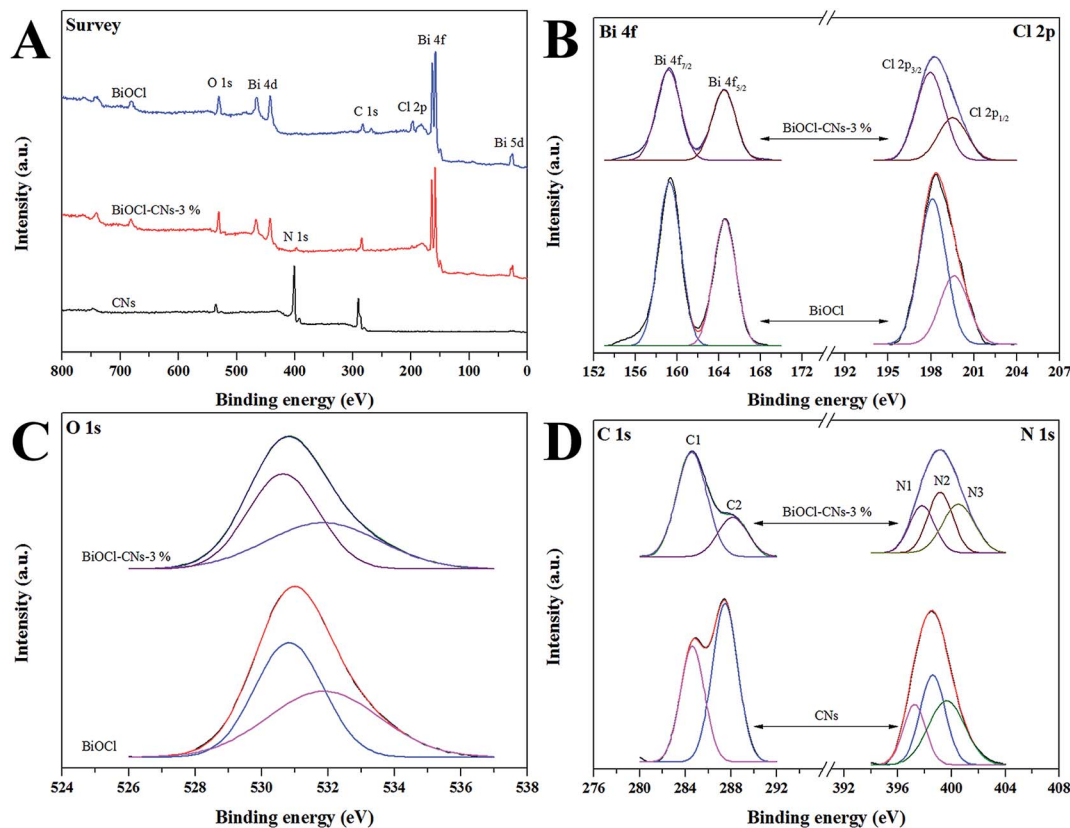


Fig. 6 X-ray photoelectron spectra of (A) survey scan of BiOCl-CNs-3% hybrid, bare BiOCl, and CNs; high-resolution spectra of (B) Bi 4f and Cl 2p of BiOCl-CNs-3% hybrid and bare BiOCl, (C) O 1s of BiOCl-CNs-3% hybrid and bare BiOCl, and (D) C 1s and N 1s of BiOCl-CNs-3% hybrid and bare CNs.

from a Bi–O bond and chemisorbed H₂O molecules or OH[−] groups on the surface, respectively.^{37,39,40} However, the binding energy values of Bi 4f_{7/2}, Bi 4f_{5/2}, Cl 2p_{3/2}, Cl 2p_{1/2}, and O 1s of BiOCl–CNs-3% hybrid are 158.9 eV, 164.2 eV, 197.9 eV, 199.5 eV, 530.6 eV, and 531.9 eV, as shown in Fig. 6B and C. As to CNs, C 1s peaks centered at 284.6 eV (C1) and 287.4 eV (C2) are ascribed to graphitic carbon on the surface of CNs and N=C–N groups of triazine rings in Fig. 6D.^{27,41,42} And the XPS N 1s peaks include three peaks centered at 397.3 eV (N1), 398.6 eV (N2), and 399.6 eV (N3), corresponding to nitrogen sp²-bonded to carbon, the C–(NH), and C≡N bonding, respectively.^{27,41,42} The binding energy values of C2, N1, N2 and N3 of BiOCl–CNs-3% hybrid are 288.1 eV, 397.8 eV, 399.2 eV, and 400.5 eV, respectively, a little larger than those of CNs. From the XPS data, both main structures of BiOCl and CNs were well sustained after hybridization, which is in good accordance with SEM and FTIR results. In addition, slight shift for binding energy values may possibly be attributed to the intense interaction between closely contacted phases of BiOCl and CNs, revealing the formation of hetero-junction structures, also observed in TEM images.

3.5 Optical property

UV-vis DRS was measured to analyze the optical absorption of bare BiOCl, CNs, and BiOCl–CNs hybrids, shown in Fig. 7A. The main absorption edge of bare BiOCl and CNs occurs at ~360 nm and ~435 nm. The band gap energy of semiconductors can be calculated as the base of the following formula:

$$\alpha h\nu = A(h\nu - E_g)^n \quad (1)$$

where α , h , ν , E_g , and A are absorption coefficient, Planck constant, light frequency, band gap energy, and a constant, respectively; n is determined by the type of optical transition of a semiconductor ($n = 1$ for direct transition and $n = 4$ for indirect transition). For bare BiOCl and g-C₃N₄ sample, values of n are 4 and 1, respectively.^{5,17} As can be seen in the inset of Fig. 7A, E_g values of synthesized bare BiOCl and CNs are estimated to be 3.30 eV and 2.97 eV, respectively, determined from a plot of

$(\alpha h\nu)^{n/2}$ versus $h\nu$. The absorption edge does not shift for all BiOCl–CNs hybrids, but extend the absorbance to the visible light region due to the presence of CNs, indicating its possible application as a visible-light-driven photocatalyst.

The band edge position of a semiconductor can be calculated according to the following empirical formulae:^{20,43}

$$E_{CB} = \chi - E^e - 0.5E_g \quad (2)$$

$$E_{VB} = E_{CB} + E_g \quad (3)$$

where E_{CB} is the conduction band (CB) edge potential; χ is the electronegativity, a geometric mean of the absolute electronegativity of the constituent atoms, expressed as the arithmetic mean of the atomic electron affinity and the first ionization energy; E^e is the energy of free electrons or the hydrogen scale (~4.5 eV); E_g is the band gap energy; E_{VB} is the valence band (VB) edge potential. The χ values for BiOCl and CNs are 6.36 and 4.73 eV, respectively. The E_{VB} of bare BiOCl and CNs can be determined to be +3.51 eV and +1.71 eV, respectively, and the corresponding E_{CB} of bare BiOCl and CNs can be estimated to be +0.21 eV and −1.26 eV, respectively. Clearly, BiOCl and CNs hold well matched band gap structures that are favorable to integrate into a same structure, facilitating the efficient utilization of photogenerated holes and electrons.

Photoluminescence spectra analysis was also applied to reveal the migration of charge carriers in semiconductors.^{17,44} Since bare CNs and BiOCl have different emission peaks, we compared them with BiOCl–CNs-3% in different wavelength ranges, as shown in Fig. 7B and its inset. The emission peak of CNs, centered at around 436 nm in visible light range, is in good accordance with the band gap of CNs. The emission band position of BiOCl–CNs-3% hybrid is similar to that of CNs, while the intensity of BiOCl–CNs-3% emission peak is greatly weakened. A same observation is also found in the UV light range. The PL intensity of BiOCl–CNs-3% hybrid is much lower than that of bare BiOCl. Based upon the PL analysis, it is evident that the recombination of charge carriers is greatly suppressed in

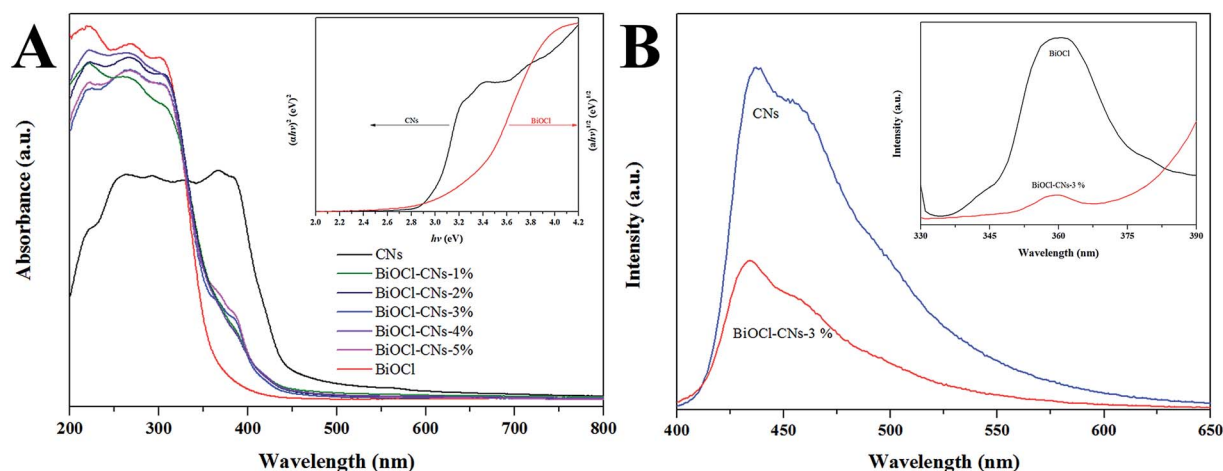


Fig. 7 (A) UV-vis diffuse reflectance spectra of BiOCl–CNs hybrids, bare BiOCl, and CNs (inset is $(\alpha h\nu)^2$ or $(\alpha h\nu)^{1/2}$ versus E_g plot of bare CNs and BiOCl); (B) photoluminescence spectra of BiOCl–CNs-3% hybrid, bare BiOCl, and CNs in different wavelength ranges.

BiOCl–CNs-3% hybrid, mainly attributing to the formation of heterojunction structures by which the efficient separation of charge carriers is achieved.

3.6 Photocatalytic activity

The photocatalytic activity of BiOCl–CNs hybrids was evaluated through decomposing dye RhB under visible light irradiation, as shown in Fig. 8A. Photolysis of RhB is almost negligible. The bare BiOCl and CNs alone can decompose RhB by 83.5% and 16.2% after 40 min, respectively. In the case of BiOCl–CNs hybrids, the photocatalytic activity is gradually enhanced with loading amount of CNs increasing from 1% to 3%. Significantly, the BiOCl–CNs-3% hybrid exhibited the highest photocatalytic efficiency towards RhB degradation since it may induce *ca.* 100% removal within 40 min. However, further increase of CNs loading amount in BiOCl–CNs hybrid up to 5% contrarily leads to a decrease of photocatalytic efficiency, possibly attributing to the fact that excess amount of CNs into BiOCl phase tends to self-agglomerate, thus suppressing the formation of heterojunction structures and decreasing the utilization of visible light.^{43,45} The low charges transfer and separation accordingly results into the decrease of photocatalytic outcome. As a result, a suitable proportion and good dispersion of CNs in the BiOCl region are necessary for the enhancement of photocatalytic performance. In addition, the photocatalytic capability of BiOCl–CNb-3% is much lower than that of BiOCl–CNs-3% in Fig. S7,[†] revealing that CNs with unique physicochemical features is a much better candidate to construct hybrids with BiOCl than bulk g-C₃N₄. During photocatalysis, a blue shift of main adsorption peak of RhB with prolonging the irradiation time was found and attributed to the gradual deethylation in Fig. S8.[†] The experimental data were fitted by a pseudo-first-order model to quantitatively investigate reaction kinetics of the RhB degradation and the corresponding apparent reaction constants (*k*) were displayed in Fig. 8B. Significantly, the BiOCl–CNs-3% exhibited the highest reaction constant that is almost 2.1 and 26.6 times as high as those of bare BiOCl and CNs alone, as also seen in Table 1.

It is notable that photocatalytic ability of mechanically ground sample BiOCl–CNs-3% (blend) is much lower than that

of BiOCl–CNs-3% hybrid and quite close to that of bare BiOCl in Fig. 8A. Similarly, the reaction constant of BiOCl–CNs-3% hybrid is nearly 1.8 times that of BiOCl–CNs-3% (blend), further implying the indeed existence of heterojunction structures between CNs and BiOCl phases, instead of the simple physical mixture. Hence, heterojunction structures can be one important factor to improve photocatalytic efficiency upon visible light illumination. Another factor to enhance photocatalysis is the unique hierarchical flowerlike units of BiOCl in morphology with enlarged specific surface area after hybridization with CNs, as seen in Table 1. The unique morphology with appropriate specific surface area ensures abundant active sites exposed and sufficient absorption of visible light, thus drastically elevating the photocatalytic efficiency.

Since the dye RhB is sensitive to visible light, its degradation is generally caused by a dye-sensitized path that does not require the band gap excitation of photocatalyst.⁴⁴ To demonstrate the visible-light-driven photocatalytic activity of BiOCl–CNs hybrids, 2,4-D was chosen as another representative colorless organic pollutant towards the catalytic evaluation, as shown in Fig. 9. During the photocatalytic process, no degradation of 2,4-D is observed in direct photolysis, indicating that 2,4-D fails to be destroyed upon visible light irradiation. The bare BiOCl is insufficient to decompose 2,4-D since BiOCl cannot be excited at the visible light region. However, 54% of

Table 1 S_{BET} , k , and correlation coefficient R of CNs–TiO₂ hybrids, bare BiOCl, and CNs

Sample	S_{BET} ($\text{m}^2 \text{g}^{-1}$)	K (min^{-1})	Correlation coefficient R
BiOCl	15.76	0.0550	0.9807
BiOCl–CNs-1%	10.21	0.0643	0.9943
BiOCl–CNs-2%	20.87	0.0677	0.9958
BiOCl–CNs-3%	19.04	0.1170	0.9914
BiOCl–CNs-4%	23.94	0.0557	0.9903
BiOCl–CNs-5%	27.19	0.0359	0.9839
BiOCl–CNs-3% (blend)	—	0.0625	0.9904
CNs	150.10	0.0044	0.9896

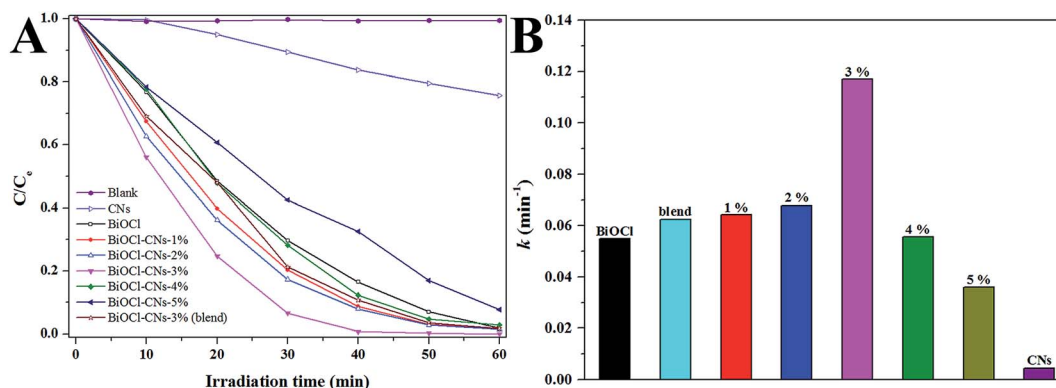


Fig. 8 (A) Photocatalytic activity for the degradation of RhB under visible light irradiation on BiOCl–CNs hybrids, bare BiOCl, and CNs; (B) comparison of apparent reaction rate (k) of corresponding photocatalysts.

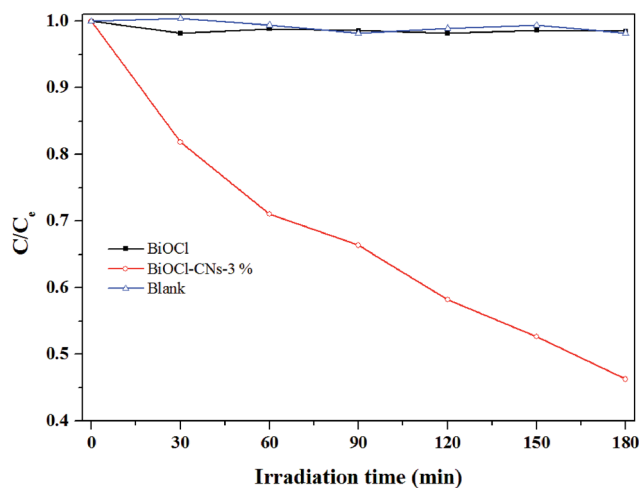


Fig. 9 Photocatalytic activity for the degradation of 2,4-D under visible light irradiation on BiOCl-CNs-3% hybrid and BiOCl.

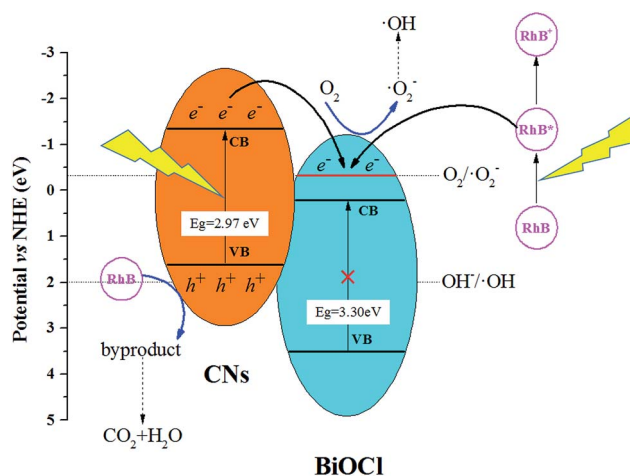
2,4-D is destroyed over BiOCl-CNs-3% hybrid after 3 h, suggesting the possibility of visible light response and thus efficient visible-light-driven catalytic performance of BiOCl-CNs-3% hybrid.

3.7 Proposed photocatalytic mechanism

It is well known that pollutants are normally deconstructed by photogenerated reactive species such as h^+ , $\cdot\text{OH}$, and $\cdot\text{O}_2^-$, and so on.^{1,20} Active species trapping and hydroxyl radical quantification experiments were therefore conducted to estimate and propose the possible photocatalytic mechanism, as shown in Fig. 10. In Fig. 10A, the photocatalytic efficiency slightly decreases upon addition of IPA, implying that radicals $\cdot\text{OH}$ are not the main active species during the reaction. It is interesting to note that, the degradation behavior of RhB is significantly hindered as soon as BQ is introduced into the catalytic system, revealing that radicals $\cdot\text{O}_2^-$ are crucial to the enhancement of photocatalytic efficiency. N_2 bubbling experiment was

conducted to expel oxygen molecules dissolved in aqueous, which would decrease entrapment of photoinduced electrons by oxygen to form $\cdot\text{O}_2^-$ radicals and thus supply low degradation efficiency. The photocatalytic outcome is also influenced to some degree by adding EDTA-2Na, certifying that holes exert important but not predominant roles. In addition, photoluminescence technique was further employed to detect the hydroxyl radicals formed on the surface of photocatalysts, as shown in Fig. 10B. It is distinct that $\cdot\text{OH}$ shows a minor effect on the photocatalytic performance under visible light irradiation, in good accordance with active species trapping experiments with IPA.

Based upon what we described above, the possible photocatalytic mechanism could be realized and proposed as Scheme 1. Under visible light irradiation ($\lambda > 400 \text{ nm}$), CNs is easily excited and produce photogenerated electron-hole pairs, whereas BiOCl fails to produce any charges due to the wide band gap (3.30 eV). Photogenerated electrons are prone to migrate from the CB of CNs to that of BiOCl since the E_{CB} of CNs



Scheme 1 Proposed mechanism of BiOCl-CNs hybrids upon visible light irradiation.

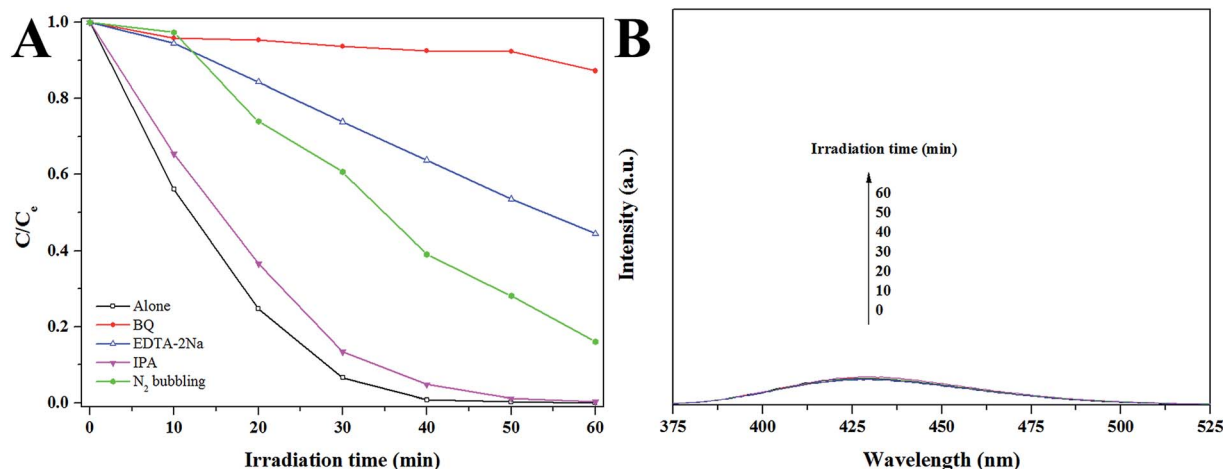


Fig. 10 (A) Active species trapping experiments and (B) hydroxyl radical quantification experiments of BiOCl-CNs-3% hybrid.

(−1.26 eV) is more negative than that of BiOCl (+0.21 eV). In addition, it is acceptable that bare BiOCl promote the degradation of dye RhB mainly owing to the effect of sensitization between BiOCl and RhB.⁴⁶ The adsorbed RhB molecules are excited to form the excited state RhB* and the excited state RhB* subsequently injected electrons to the CB of BiOCl because of the more negativity of LUMO potential (−0.75 eV) than the E_{CB} of BiOCl (+0.21 eV).⁴⁷ As an electron-relay semiconductor, BiOCl tends to accept electrons donated from CNs and RhB* at the potential (−0.33 eV) ($E_{(O_2/O_2^-)} = -1.33$ eV/NHE).⁴⁸ As a result, the electrons are able to react with oxygen molecules absorbed on the surface of BiOCl–CNs hybrids to produce radicals $\cdot O_2^-$, which was proven by the result of active species trapping experiments. The holes left on the VB of CNs cannot directly oxidize the adsorbed H₂O molecules to form $\cdot OH$ radicals, since the E_{VB} of CNs is relatively negative comparing to $\cdot OH/H_2O$ ($E_{(\cdot OH/H_2O)} = +2.38$ eV/NHE).⁴⁸ Therefore, it is reasonable to speculate that radicals $\cdot OH$ are mainly generated by a two-electron oxygen reduction route: $O_2 + 2e^- + 2H^+ \rightarrow H_2O_2 \rightarrow \cdot OH$ due to the reduction potential of O_2/H_2O_2 was 0.695 eV.⁴⁹ In this study, holes oxidize and decompose molecular RhB through a direct manner, instead of generating $\cdot OH$ radicals that further contribute to degradation. As a result, it is understandable that both photocatalytic and photosensitive routes combine and cooperate towards degradation of dye RhB as the base of above discussion.

The stability, reusability, and durability of BiOCl–CNs hybrids were finally evaluated. BiOCl–CNs-3% hybrid was specially selected and subjected to successive photocatalytic measurements. High photocatalytic capability could be even maintained after seventh cycling runs and there was no obviously catalytic deactivation, as shown in Fig. 11. In addition, no distinct variation in chemical composition, phase structure, and surface morphology was found, evidenced by the XRD, FT-IR and SEM analysis of BiOCl–CNs-3% hybrid before and after photocatalytic reaction in Fig. S9A–D.† Therefore satisfactory stability and reusability were confirmed for robust photocatalyst

BiOCl–CNs-3% hybrid, which are quite important for potential and real applications. Contrarily, bare BiOCl prepared in this study could not supply satisfactory results even used after barely one time, which mainly attributed to the destruction of hierarchical units in morphology, as shown in Fig. S9E and F.† From this aspect, we speculated that some CNs fragments might be arranged at some suitable positions as wedges among BiOCl nanoplates during preparation and thus significantly stabilized those hybrids even exposure to the photocatalytic measurements, evidenced in Fig. S9C and D.† Therefore, the CNs in our study made roles not only a sensitizer to harvest visible light, but also a stabilizer in hierarchical structures, as displayed in Fig. 11 and S9.†

4. Conclusion

A series of novel and robust BiOCl–CNs hybrids were prepared using the exfoliated g-C₃N₄ nanosheets through a facile chemical deposition-precipitation route. Structural characterization indicated that main structures of both components BiOCl and CNs were maintained and heterojunction structures were indeed formed after hybridization. The as-synthesized BiOCl–CNs hybrids were subjected to the photocatalytic measurements towards RhB degradation. It was found that all robust hybrids displayed significantly enhanced catalytic efficiency in comparison to bare BiOCl and CNs, mainly attributing to the enlarged specific surface area, favorable optical property, and suitable energy-band structure. Especially, the best candidate, hybrid BiOCl–CNs-3%, could show photocatalytic reaction rate nearly 2.1 and 26.6 times that of individual BiOCl and CNs, respectively. Possible photocatalytic mechanism was also estimated and proposed based upon active species trapping measurements, revealing that superoxide radicals ($\cdot O_2^-$) played crucial roles during photocatalytic processes.

Acknowledgements

We are grateful to the National Natural Science Foundation of China (Grant number 21207089 and 41076040), the project-sponsored by SRF for ROCS, SEM., and the 863 project (Grant number 2013AA06A207-1) for financial support.

References

- 1 Y. Tian, B. Chang, J. Lu, J. Fu, F. Xi and X. Dong, *ACS Appl. Mater. Interfaces*, 2013, **5**, 7079–7085.
- 2 F. Dong, Y. Sun, M. Fu, Z. Wu and S. C. Lee, *J. Hazard. Mater.*, 2012, **219–220**, 26–34.
- 3 N. Serpone, A. V. Emeline, S. Horikoshi, V. N. Kuznetsov and V. K. Ryabchuk, *Photochem. Photobiol. Sci.*, 2012, **11**, 1121–1150.
- 4 J. Shi, *Chem. Rev.*, 2012, **113**, 2139–2181.
- 5 K.-L. Zhang, C.-M. Liu, F.-Q. Huang, C. Zheng and W.-D. Wang, *Appl. Catal., B*, 2006, **68**, 125–129.
- 6 X. Lin, T. Huang, F. Huang, W. Wang and J. Shi, *J. Phys. Chem. B*, 2006, **110**, 24629–24634.

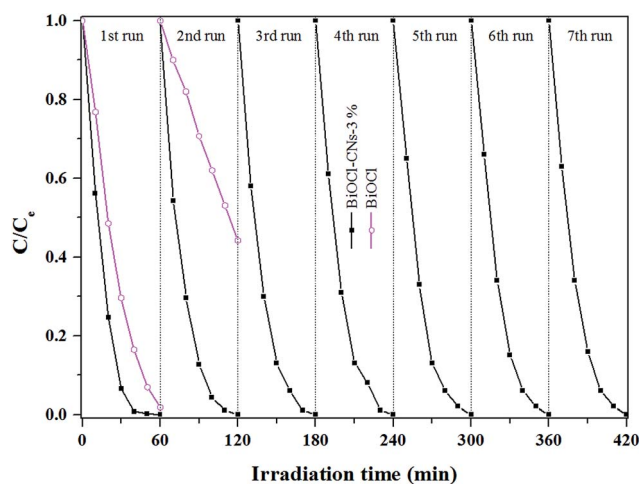


Fig. 11 Reusability of BiOCl–CNs-3% hybrid and bare BiOCl over RhB degradation.

- 7 J. Cao, B. Xu, H. Lin, B. Luo and S. Chen, *Catal. Commun.*, 2012, **26**, 204–208.
- 8 W. Yang, B. Ma, W. Wang, Y. Wen, D. Zeng and B. Shan, *Phys. Chem. Chem. Phys.*, 2013, **15**, 19387–19394.
- 9 T. B. Li, G. Chen, C. Zhou, Z. Y. Shen, R. C. Jin and J. X. Sun, *Dalton Trans.*, 2011, **40**, 6751–6758.
- 10 J. Zhang, J. Xia, S. Yin, H. Li, H. Xu, M. He, L. Huang and Q. Zhang, *Colloids Surf., A*, 2013, **420**, 89–95.
- 11 X. Chang, G. Yu, J. Huang, Z. Li, S. Zhu, P. Yu, C. Cheng, S. Deng and G. Ji, *Catal. Today*, 2010, **153**, 193–199.
- 12 X. Wang, K. Maeda, A. Thomas, K. Takanebe, G. Xin, J. M. Carlsson, K. Domen and M. Antonietti, *Nat. Mater.*, 2009, **8**, 76–80.
- 13 T. Li, L. Zhao, Y. He, J. Cai, M. Luo and J. Lin, *Appl. Catal., B*, 2013, **129**, 255–263.
- 14 Y. Wang, X. Wang and M. Antonietti, *Angew. Chem., Int. Ed.*, 2012, **51**, 68–89.
- 15 F. Su, S. C. Mathew, G. Lipner, X. Fu, M. Antonietti, S. Blechert and X. Wang, *J. Am. Chem. Soc.*, 2010, **132**, 16299–16301.
- 16 H. Yan, *Chem. Commun.*, 2012, **48**, 3430–3432.
- 17 P. Niu, L. Zhang, G. Liu and H.-M. Cheng, *Adv. Funct. Mater.*, 2012, **22**, 4763–4770.
- 18 J. Xu, L. Zhang, R. Shi and Y. Zhu, *J. Mater. Chem. A*, 2013, **1**, 14766–14772.
- 19 S. Yang, Y. Gong, J. Zhang, L. Zhan, L. Ma, Z. Fang, R. Vajtai, X. Wang and P. M. Ajayan, *Adv. Mater.*, 2013, **25**, 2452–2456.
- 20 L. Ye, J. Liu, C. Gong, L. Tian, T. Peng and L. Zan, *ACS Catal.*, 2012, **2**, 1677–1683.
- 21 C. Pan, J. Xu, Y. Wang, D. Li and Y. Zhu, *Adv. Funct. Mater.*, 2012, **22**, 1518–1524.
- 22 S. Shi, M. A. Gondal, A. A. Al-Saadi, R. Fajgar, J. Kupcik, X. Chang, K. Shen, Q. Xu and Z. S. Seddigi, *J. Colloid Interface Sci.*, 2014, **416**, 212–219.
- 23 X. Wang, Q. Wang, F. Li, W. Yang, Y. Zhao, Y. Hao and S. Liu, *Chem. Eng. J.*, 2013, **234**, 361–371.
- 24 K. Maeda, K. Teramura, D. Lu, T. Takata, N. Saito, Y. Inoue and K. Domen, *Nature*, 2006, **440**, 295.
- 25 K. Maeda, H. Hashiguchi, H. Masuda, R. Abe and K. Domen, *J. Phys. Chem. C*, 2008, **112**, 3447–3452.
- 26 X. Hu, T. Mohamood, W. Ma, C. Chen and J. Zhao, *J. Phys. Chem. B*, 2006, **110**, 26012–26018.
- 27 F. Chang, Y. Xie, C. Li, J. Chen, J. Luo, X. Hu and J. Shen, *Appl. Surf. Sci.*, 2013, **280**, 967–974.
- 28 Y. Xie, F. Chang, C. Li, J. Chen, J. Luo, L. Li and X. Hu, *Clean: Soil, Air, Water*, 2014, **42**, 521–527.
- 29 N. Cheng, J. Tian, Q. Liu, C. Ge, A. H. Qusti, A. M. Asiri, A. O. Al-Youbi and X. Sun, *ACS Appl. Mater. Interfaces*, 2013, **5**, 6815–6819.
- 30 L. Chen, D. Huang, S. Ren, T. Dong, Y. Chi and G. Chen, *Nanoscale*, 2013, **5**, 225–230.
- 31 L. Zhang, W. Wang, L. Zhou, M. Shang and S. Sun, *Appl. Catal., B*, 2009, **90**, 458–462.
- 32 C. Han, L. Ge, C. Chen, Y. Li, X. Xiao, Y. Zhang and L. Guo, *Appl. Catal., B*, 2014, **147**, 546–553.
- 33 S. C. Yan, Z. S. Li and Z. G. Zou, *Langmuir*, 2009, **25**, 10397–10401.
- 34 G. Liao, S. Chen, X. Quan, H. Yu and H. Zhao, *J. Mater. Chem.*, 2012, **22**, 2721–2726.
- 35 H. Kato and A. Kudo, *Chem. Phys. Lett.*, 1998, **295**, 487–492.
- 36 A. Thomas, A. Fischer, F. Goettmann, M. Antonietti, J.-O. Muller, R. Schlögl and J. M. Carlsson, *J. Mater. Chem.*, 2008, **18**, 4893–4908.
- 37 J.-M. Song, C.-J. Mao, H.-L. Niu, Y.-H. Shen and S.-Y. Zhang, *CrystEngComm*, 2010, **12**, 3875–3881.
- 38 L. Ye, K. Deng, F. Xu, L. Tian, T. Peng and L. Zan, *Phys. Chem. Chem. Phys.*, 2012, **14**, 82–85.
- 39 L. Armelao, G. Bottaro, C. Maccato and E. Tondello, *Dalton Trans.*, 2012, **41**, 5480–5485.
- 40 S. Peng, L. Li, P. Zhu, Y. Wu, M. Srinivasan, S. G. Mhaisalkar, S. Ramakrishna and Q. Yan, *Chem.-Asian J.*, 2013, **8**, 258–268.
- 41 X. Wang, X. Chen, A. Thomas, X. Fu and M. Antonietti, *Adv. Mater.*, 2009, **21**, 1609–1612.
- 42 S. C. Yan, Z. S. Li and Z. G. Zou, *Langmuir*, 2010, **26**, 3894–3901.
- 43 H. Xu, J. Yan, Y. Xu, Y. Song, H. Li, J. Xia, C. Huang and H. Wan, *Appl. Catal., B*, 2013, **129**, 182–193.
- 44 K. Zhang, J. Liang, S. Wang, J. Liu, K. Ren, X. Zheng, H. Luo, Y. Peng, X. Zou, X. Bo, J. Li and X. Yu, *Cryst. Growth Des.*, 2011, **12**, 793–803.
- 45 J. Lu, I. Do, L. T. Drzal, R. M. Worden and I. Lee, *ACS Nano*, 2008, **2**, 1825–1832.
- 46 J. He, G. Benkő, F. Korodi, T. Polívka, R. Lomoth, B. Åkermark, L. Sun, A. Hagfeldt and V. Sundström, *J. Am. Chem. Soc.*, 2002, **124**, 4922–4932.
- 47 J. Fu, Y. Tian, B. Chang, F. Xi and X. Dong, *J. Mater. Chem.*, 2012, **22**, 21159–21166.
- 48 J. Jiang, H. Li and L. Zhang, *Chem.-Euro. J.*, 2012, **18**, 6360–6369.
- 49 J. Kim, C. W. Lee and W. Choi, *Environ. Sci. Tech.*, 2010, **44**, 6849–6854.